PNAS Nexus, 2024, 3, pgae484
https://doi.org/10.1093/pnasnexus/pgae484
Advance access publication 27 October 2024
Research Report

Asymmetric fluctuation of overlapping dinucleosome studied by cryoelectron microscopy and small-angle X-ray scattering

Masahiro Shimizu [a,1], Hiroki Tanaka [b,1], Masahiro Nishimura [b,1], Nobuhiro Sato [a,1], Kayo Nozawa [b,2], Haruhiko Ehara [c], Shun-ichi Sekine [c], Ken Morishima [a], Rintaro Inoue [a], Yoshimasa Takizawa [b], Hitoshi Kurumizaka [b,*] and Masaaki Sugiyama [a,*]

[a]Laboratory of Radiation Material Science, Institute for Integrated Radiation and Nuclear Science, Kyoto University, 2-1010, Kumatori, Sennan-gun, Osaka 590-0494, Japan
[b]Laboratory of Chromatin Structure and Function, Institute for Quantitative Biosciences, The University of Tokyo, 1-1-1 Yayoi, Bunkyo-ku, Tokyo 113-0032, Japan
[c]Laboratory for Transcription Structural Biology, RIKEN Center for Biosystems Dynamics Research, 1-7-22 Suehiro-cho, Tsurumi-ku, Yokohama 230-0045, Japan
*To whom correspondence should be addressed: Email: kurumizaka@iqb.u-tokyo.ac.jp (H.K.); Email: sugiyama.masaaki.5n@kyoto-u.ac.jp (M.Su.)
[1]M.S., H.T., M.N., and N.S. contributed equally to this work.
[2]School of Life Science and Technology, Tokyo Institute of Technology, Yokohama, Kanagawa 226-8501, Japan
Edited By Ivet Bahar

Abstract

Nucleosome remodelers modify the local structure of chromatin to release the region from nucleosome-mediated transcriptional suppression. Overlapping dinucleosomes (OLDNs) are nucleoprotein complexes formed around transcription start sites as a result of remodeling, and they consist of two nucleosome moieties: a histone octamer wrapped by DNA (octasome) and a histone hexamer wrapped by DNA (hexasome). While OLDN formation alters chromatin accessibility to proteins, the structural mechanism behind this process is poorly understood. Thus, this study investigated the characteristics of structural fluctuations in OLDNs. First, multiple structures of the OLDN were visualized through cryoelectron microscopy (cryoEM), providing an overview of the tilting motion of the hexasome relative to the octasome at the near-atomistic resolution. Second, small-angle X-ray scattering (SAXS) revealed the presence of OLDN conformations with a larger radius of gyration than cryoEM structures. A more complete description of OLDN fluctuation was proposed by SAXS-based ensemble modeling, which included possible transient structures. The ensemble model supported the tilting motion of the OLDN outlined by the cryoEM models, further suggesting the presence of more diverse conformations. The amplitude of the relative tilting motion of the hexasome was larger, and the nanoscale fluctuation in distance between the octasome and hexasome was also proposed. The cryoEM models were found to be mapped in the energetically stable region of the conformational distribution of the ensemble. Exhaustive complex modeling using all conformations that appeared in the structural ensemble suggested that conformational and motional asymmetries of the OLDN result in asymmetries in the accessibility of OLDN-binding proteins.

Keywords: chromatin, chromatin remodeler, molecular dynamics simulation, ensemble modeling

Significance Statement

Cryoelectron microscopy (cryoEM) visualizes multiple conformations of a biomolecule at the near-atomistic resolution to elucidate its functional motion. Although chemical cross-linking is useful to obtain high-resolution models through cryoEM, there is still a lack of research on biases in resultant structures caused by sample processing. Here, the structural fluctuation of the overlapping dinucleosome (OLDN), a nucleoprotein complex formed around the transcription start site, was investigated by combining cryoEM and small-angle X-ray scattering (SAXS). The 12 cryoEM models obtained from the OLDN with chemical cross-linking were mapped to energetically stable structures in the SAXS-based structural ensemble. Our results suggest that combining structural data from cryoEM and SAXS provides complementary insights, leading to a more comprehensive understanding of dynamic biomolecules.

Introduction

Eukaryotic chromatin is compact and dynamic, enabling controlled and timely transcription from the appropriate DNA region (1). The functional dynamics of chromatin span a wide hierarchy. The nucleosome is a fundamental structural unit in chromatin that accommodates the entire genomic DNA within the cell

Competing Interest: The authors declare that they have no competing interests.
Received: May 10, 2024. **Accepted:** October 12, 2024

nucleus (2). Histones H2A, H2B, H3, and H4 are protein components of the nucleosome (3). In the canonical nucleosome, the histone octamer containing the two H2A–H2B and H3–H4 heterodimers are lefthandedly wrapped with 150 base pairs of DNA (4). This stable nucleosomal structure generally inhibits genomic function in chromatin. For example, nucleosomes formed around the transcription start site (TSS) suppress the initiation of gene expression (5). This may be because nucleosome formation substantially inhibits the assembly of DNA-binding proteins required for transcription initiation around the TSS (6). To resolve nucleosome-mediated transcriptional suppression, nucleosome remodelers are recruited around the TSS, and an overlapping dinucleosome (OLDN) may be formed as a consequence of the nucleosome remodeling reaction (7). The atomic structure of the OLDN, which comprises an octasome and a hexasome, has been revealed using X-ray crystallography (8). The octasome encompasses the histone octamer as a canonical nucleosome, whereas the hexasome lacks one H2A–H2B dimer compared with the octasome. In addition, the structural flexibility of OLDNs has also been proposed (9).

However, the impact of OLDN formation on chromatin structure and properties is not yet fully understood. In chromatin, OLDNs should continually change their conformation by external force from the connected DNA regions and neighboring nucleosomes. Furthermore, it is not yet clear how OLDNs, the result of nucleosome remodeling, enhance the accessibility of other functional proteins to chromatin.

Although it is difficult to observe OLDNs in chromatin directly at the atomistic resolution, trends in the fluctuation and deformation of a single OLDN should provide information on their dynamics under external force. Structural biology has recently made significant strides in understanding structural fluctuations by integrating various methods. One distinguished method, cryoelectron microscopy (cryoEM), has become an indispensable tool for capturing real images of biomacromolecules with high spatial resolution without sample crystallization. Furthermore, this method often provides multiple high-resolution structures of a biomolecule, providing insights into its molecular motion (10). From a different perspective, methods for visualizing molecular motion by coupling measurements with computational simulations have also been evolving. Solution scattering techniques, such as small-angle X-ray scattering (SAXS) and small-angle neutron scattering, provide averaged scattering profiles of all possible structures of a dynamic biomolecule, including transient and rare structures. Nevertheless, individual conformations that make up a molecular motion cannot be solved from an experimental scattering profile alone, because it cannot be decomposed into profiles of the individual structures. Advances in ensemble modeling methods have overcome this limitation by providing a structural set representing a biomolecular motion, incorporating both experimental scattering data and a biomolecular force field (11–15). Therefore, the integration of cryoEM, solution scattering, and ensemble modeling methods is expected to encompass the entire range of conformations of the fluctuating biomacromolecule.

Following the above-mentioned strategy, we employed cryoEM, SAXS, and coarse-grained molecular dynamics (CG-MD) simulations to visualize the structural fluctuations of the OLDN. First, by collecting multiple cryoEM images of the OLDN as snapshots, we gained insights into its mode of motion, including the characteristics of the distance and direction between two nucleosomal moieties. Second, to reveal the fluctuating structures in more detail, we conducted ensemble modeling using SAXS and CG-MD simulations, which allowed us to analyze the distribution range of the fluctuating structures. Through this integrated analysis, we propose an overall picture of the structural fluctuations in the OLDN. Finally, a possible mechanism of OLDN formation is discussed.

Results

Fluctuation of the OLDN visualized by cryoEM

Reconstituted OLDN samples were purified by native polyacrylamide gel electrophoresis (PAGE) using a PrepCell apparatus (SI Appendix Fig. S1). The OLDN samples were fractionated by sucrose gradient ultracentrifugation with glutaraldehyde fixation (GraFix) (16) (Fig. S1). Each OLDN sample was then subjected to data collection using a 200 kV electron microscope, and 1.5 million particles were identified from 3,000 electron micrographs (Fig. S2). We initially obtained twelve 3D classes of the OLDN structures (classes 01–12). The hexasome and octasome moieties of the OLDN were commonly observed in these 12 classes (Fig. 1A). To compare the hexasome–octasome arrangements among OLDN structures, we superimposed these 12 low-resolution structures, which involved fitting the octasome units to one another. Through this process, we confirmed structural fluctuations that were diverse spatial arrangements of the hexasome unit relative to the octasome unit (Fig. 1B).

To clarify the structural details of the hexasome–octasome arrangement in the OLDN, we performed multibody refinement separately for the hexasome and octasome units (Figs. 2A and S2). Four representative models are selectively shown in Fig. 2A. Class 01 represented the closed form, in which the hexasome and octasome moieties were in close proximity. In contrast, class 09 represented the open form, in which the hexasome and

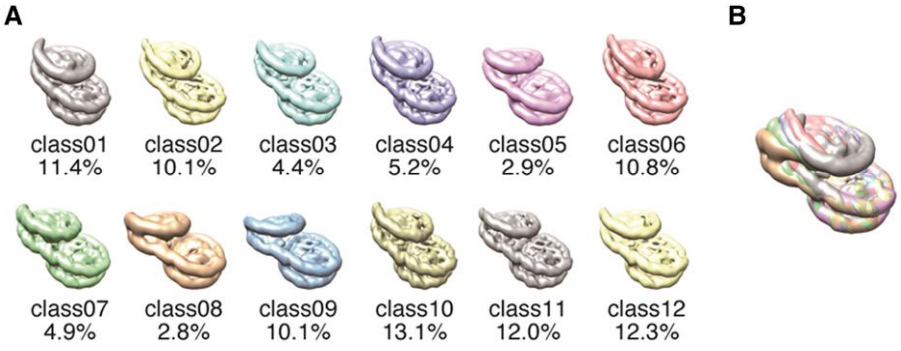

Fig. 1. Multiple cryoEM density maps of the OLDN. A) 12 cryoEM density maps (classes 01–12) obtained by 3D classification from 1.3 million particles. The percentage of particles in each class is shown below the map. B) Superimposition of the 12 cryoEM density maps aligned by the octasome moiety.

octasome moieties were spatially separated. Classes 06 and 10 were intermediate forms between classes 01 and 09. Subsequently, we obtained atomic models for these cryoEM structures. Consistent with the previously described crystal structure (8), in all four structures, one H2A–H2B dimer was absent at the hexasome–octasome interface (Fig. 2B), and the hexasomal

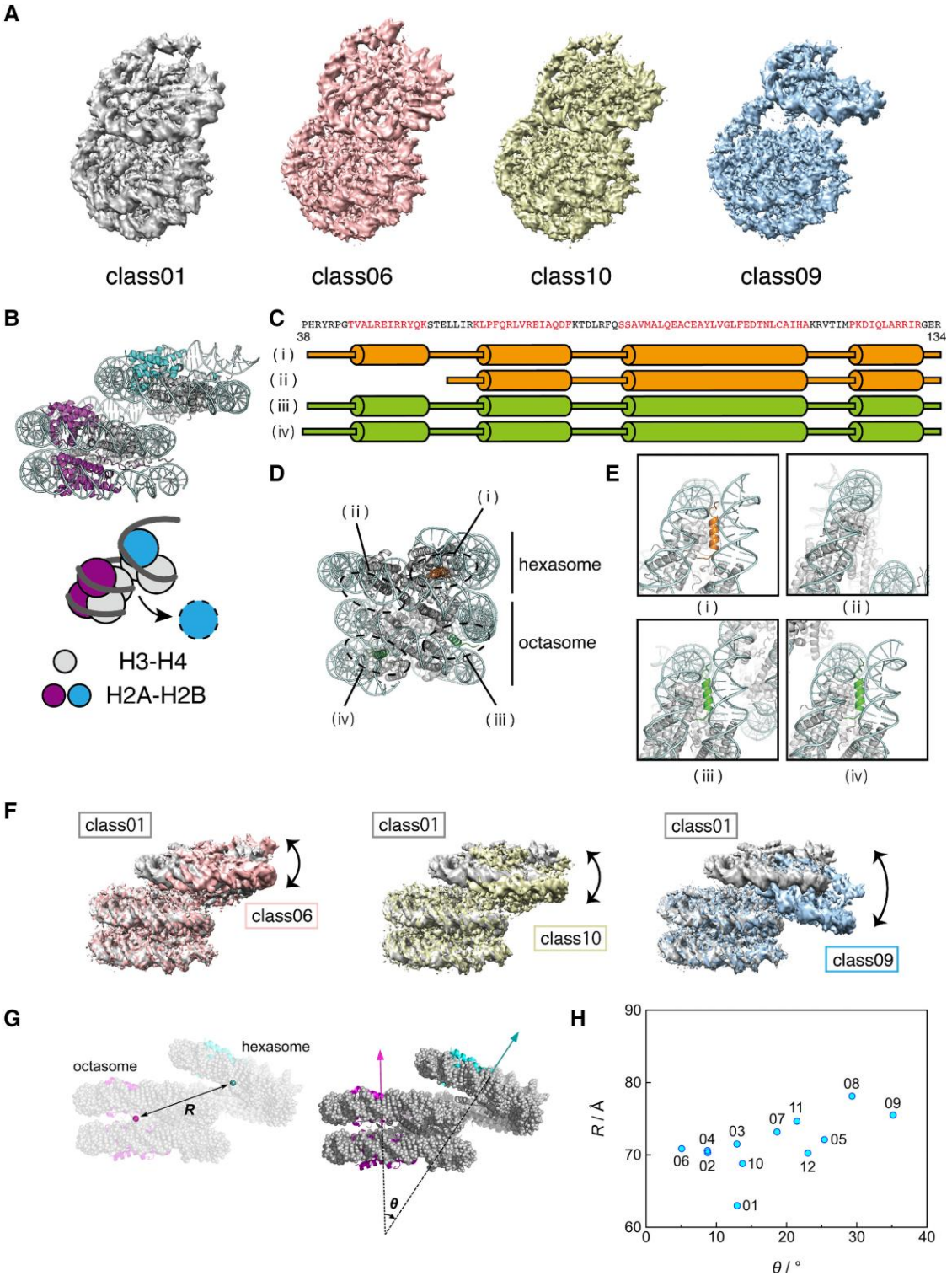

Fig. 2. Structural details of the OLDN obtained by cryoEM analysis. A) Refined cryoEM density maps of the OLDN structures. The closed form (class 01), intermediate forms (classes 06 and 10), and open form (class 09) are shown in gray, pink, yellow, and blue, respectively. B) The atomic model of OLDN class 10. The H2A–H2B dimers in the hexasome and octasome moieties are shown in cyan and magenta, respectively. C) The amino acid residues and the secondary structures of H3.1 visible in the cryoEM structure of the OLDN. H3.1 molecules in the hexasome and octasome are colored orange (i and ii) and green (iii and iv), respectively. D) Locations of the H3 αN helices in the OLDN. The H3 αN helices labeled with (i), (ii), (iii), and (iv) correspond to the H3.1 molecules shown in C). E) Close-up views of four H3 αN helices (i, ii, iii, and iv) in the OLDN. F) Angular differences of the hexasome–octasome stackings between class 01 (gray) and each of class 06 (pink), class 09 (blue), and class 10 (yellow). G) Distance of center of geometry between two nucleosome moieties R and the angle of their planar orientation θ. H) Distribution of cryoEM models.

H3 αN helix facing the interface was disordered (Fig. 2C–E). Therefore, the unique structural features of the OLDN found in the crystal structure were maintained in a solution, as shown in the cryoEM structures. The structural differences between open and intermediate conformations, or open and closed forms, are described in Fig. 2F. To quantitatively understand this motion, we focused on the distance of the center of geometry R and the angle of normal vectors θ between the planes of the hexasome and octasome units (Fig. 2G, definition details described in the SI Appendix), the structural distribution of all cryoEM structures is mapped in Fig. 2H. In summary, the cryoEM models were distributed in the ranges of $R = 62$–78 Å and $\theta = 15$–$35°$, which reflected the structural fluctuations of the OLDN in solution.

Fluctuation of OLDN in solution visualized by ensemble modeling based on SAXS and CG-MD simulations

To estimate the conformational ensemble of the fluctuating structures of OLDN, we conducted SAXS, which corresponded to the average structure over the conformational ensemble. Figure 3A shows the experimental SAXS profile for the OLDN after analytical ultracentrifugation (AUC)-SAXS treatment (17, 18), which removed the contribution of 1.7% of aggregated components in the sample solution (Fig. S3). Furthermore, dynamic light scattering (DLS) was performed to confirm that the sample did not contain large aggregates (1.5 MDa), which were outside the range of the current AUC measurement (Fig. S4). Figure 3B shows the Guinier plot and the result of the least-square fitting with the Guinier formula, $I(q) = I_0 \exp(-R_g^2 q^2/3)$, where I_0 and R_g are the forward scattering intensity and radius of gyration, respectively. From the Guinier fitting, R_g was found to be 55.0 ± 0.5 Å.

The calculated SAXS profiles of the 12 cryoEM models were compared with the experimental SAXS profiles, as shown in Fig. S5A. The values of χ^2 and gyration radii are listed in Table 1. The χ^2 value is an index indicating the degree of agreement between the calculated SAXS profile $I_{cal}(q)$ and the experimental SAXS one $I_{exp}(q)$: $\chi^2 = 1/(N-1)\sum_i^N ((I_{cal}(q_i) - I_{exp}(q_i))/\sigma_i)^2$, where N, q_i, and σ_i are the number of measurement points, scattering vector of i th measurement point, and its experimental error, respectively. All χ^2 values were relatively large, indicating that neither cryoEM model alone matched the structure reflecting the SAXS data. Because of the smaller R_g values of the cryoEM models than the experimental R_g value (Table 1), any mixture of the 12 structures cannot reproduce the experimental SAXS profile. Thus, there should be different structures in the solution compared with the 12 models solved by cryoEM.

A structure set that contains 12 cryoEM models and reproduces the SAXS profile is expected to be one of the following two possible structure sets. First, the 12 cryoEM models almost cover a distribution range of fluctuating structures of the OLDN. In this possibility, the OLDN exists mostly as an intermediate state between these 12 cryoEM structures. Second, the OLDN fluctuates more widely than the open–close motion observed by cryoEM models. The schematic views of the two possibilities are shown in Fig. S6.

When the structural distribution of the OLDN follows the first possibility, a structure that reproduces the experimental

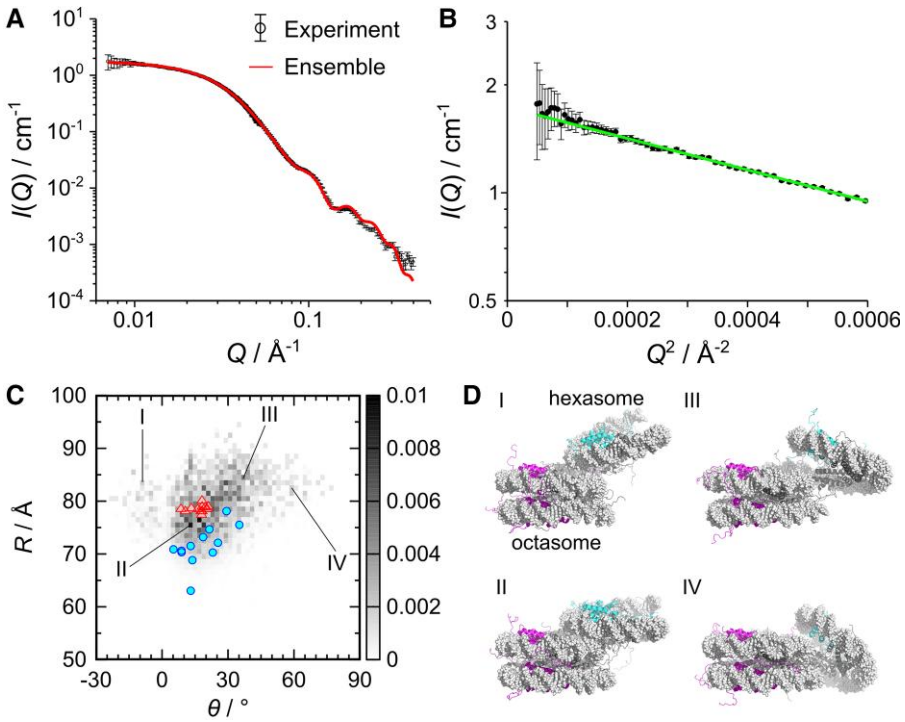

Fig. 3. Ensemble modeling of the OLDN from the SAXS profile and CG-MD simulation. A) Experimental SAXS profile of the OLDN (open circles) and theoretical SAXS profile of the SAXS- and CG-MD-based ensemble model (red line). In the experimental profile, the contribution of unintended oligomers or degradation products of the OLDN was removed by AUC-SAXS treatment (17, 18). B) Guinier plot of the experimental SAXS profile. The fitted line is shown in green. In (A) and (B), error bars represent the SD. C) Two-dimensional histogram of the geometrical parameters of the structural ensemble based on SAXS and CG-MD simulations. The scale bar indicates the probability. The values of the cryoEM models (cyan circles) and the NMA-optimized models (pink triangles) are also shown. D) Representative structures in the structural ensemble. Their corresponding θ and R are shown in C) with lines and text. DNA, H3–H4 heterodimers, H2A–H2B heterodimers in the octasome, and H2A–H2B heterodimers in the hexasome are shown by gray spheres, gray ribbon, magenta ribbon, and cyan ribbon, respectively.

Table 1. χ^2 and R_g of the 12 OLDN models.

Class	χ^2		R_g/Å	
	CryoEM models	NMA optimization	CryoEM models	NMA optimization
1	110	4.9	49.1	56.9
2	32	4.7	51.3	56.0
3	26	3.8	51.7	56.2
4	31	3.7	51.4	56.2
5	20	3.9	52.0	56.2
6	30	6.0	51.5	55.8
7	19	4.9	52.6	56.3
8	7.5	2.7	54.5	57.0
9	9.9	5.1	53.5	56.2
10	44	4.1	50.8	56.2
11	13	4.0	53.2	56.4
12	30	3.7	51.3	57.1

SAXS profile, namely an averaged structure, should exist in the distribution range of the cryoEM models. Therefore, to explore the structural models of the OLDN that matched the SAXS profile, we employed a structural optimization method with a normal mode analysis (NMA-optimization method). In the NMA-optimization method, an initial structure is modulated into another structure utilizing small normal mode vectors, followed by calculating their SAXS profiles and their χ^2 values for the experimental SAXS profile. Then, the structure with the lower χ^2 value yields the initial structure for the next round of the optimization. This operation is iteratively performed until the χ^2 value is sufficiently small and the final structure is adopted. The details of the NMA-optimization method with Pepsi-SAXS software (19) are outlined in the Supporting Methods in the SI Appendix. In this study, by adopting each of the 12 cryoEM models as the initial structure, the NMA-optimization method found each of the 12 optimized structures. As shown in Fig. S5B, their SAXS profiles were well-fitted to the experimental ones, and their χ^2 and R_g values are listed in Table 1. Figure S5C shows the structural distribution of the 12 optimized structures (pink circles), referring to their initial cryoEM structures (numbered cyan circles). All the NMA-optimized structures were concentrated in the narrow region with $R \sim 75$ Å and $10^{\circ} < \theta < 20^{\circ}$. Unlike the first possibility, this region is outside the distribution region of cryoEM models, where $R < 75$ Å and $5^{\circ} < \theta < 35^{\circ}$. Consequently, the first possibility was not plausible.

Subsequently, we addressed the second possibility, in which the OLDN fluctuated significantly around the conformation of the 12 cryoEM models, which were visualized as quasi-stable structures. To describe these structural fluctuations in the OLDN, structural sampling using CG-MD simulations was integrated with the experimental SAXS profile. It has been reported that Kullback–Leibler divergence is useful for modeling a structural ensemble that matches both the small-angle scattering profile and CG-MD simulations (20), where the Kullback–Leibler divergence indicates the difference between a structural distribution obtained by CG-MD and a resultant distribution. Referring to this idea, we adopted Kullback–Leibler divergence as a criterion for modeling fluctuations in the OLDN. The modeling was performed using a simple gradient method. First, the initial structural ensemble was obtained through CG-MD simulations. Second, the ensemble was gradually and repeatedly modified until $\chi^2 < 3.0$. In each operation, one snapshot was selected, and its weight was slightly reduced. The reweighted snapshot was selected based on $\frac{\Delta\chi_j^2}{\Delta KL_j}$, where $\Delta\chi_j^2$ is the change in χ^2 when the weight of the jth snapshot is reduced, and ΔKL_j is the change in KL according to the reweighting (more detail in the Materials and methods section). Through this procedure, a conformation ensemble of OLDN with $\chi^2 = 3.0$ was obtained. The χ^2 value is smaller than that of any NMA-optimized model. Figure 3C shows the structural distribution of the OLDN. The obtained ensemble not only covered the distribution region of the 12 cryoEM models but also expanded to the range of $R \sim 90$ Å and $\theta \sim 60^{\circ}$. That is, the amplitude of the open–close motion of the OLDN was greater than that expected by the cryoEM models, and the tilting motion of the hexasome relative to the octasome appeared more clearly. The representative structures in the (θ, R) map are shown in Fig. 3D. Deviation along the R was considerably larger than that expected from the cryoEM models. Regardless of whether the θ resembled the open or closed structure of the cryoEM models, structures with a larger R appeared at a high frequency. Finally, the robustness of the ensemble model to the initial structural distribution was confirmed by performing the same approach using a smaller initial structural set, which was obtained by dividing the original set of CG-MD simulations into five structural sets (Fig. S7). We also confirmed that the ionic strength parameter for CGMD had little effect on the ensemble, at least in the range of 0.1 to 0.175 (Fig. S8).

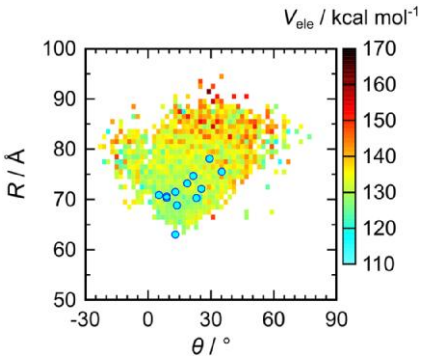

Fig. 4. Electrostatic potential energy (V_{ele}) of the OLDN in the SAXS-based structural ensemble. Distribution of the average electrostatic potential energy is shown. The (θ, R) of the 12 cryoEM models (cyan circles) are also shown. Here, the potential energy was shown for pixels with an appearance probability >0.0001 in Fig. 3C.

Interpretation of the difference in structural diversity of the OLDN between cryoEM and SAXS-based structural ensemble

To interpret the difference between the SAXS-based structural distribution and that of the cryoEM models (Fig. 3C), we investigated whether the 12 cryoEM models were located in relatively stable states in the SAXS- and CG-MD-based conformational distribution. Since many cryoEM images are required to obtain a high-resolution model, it was expected that the obtained 12 models would fluctuate less or be relatively stable among the possible conformations.

Since an electrostatic interaction is dominant between the octasome and the hexasome under the CG-MD force field, the stability of the OLDN was estimated using the electrostatic potential. Figure 4 maps the averaged electrostatic potential in the (θ, R)-space. The results mostly supported our perspective that the 12 cryoEM models were located in a region with relatively low electrostatic potential, that is, a stable region. Meanwhile, the noncryoEM-observable structures were distributed in relatively

higher potential regions (orange and red) in the conformational ensemble.

Accessibility of the nucleosome remodeler to the OLDN

Finally, the accessibility of possible OLDN-binding for OLDN was examined. SWI/SNF (switch/sucrose nonfermentable) remodelers are OLDN-binding proteins, which are involved in the OLDN formation (7). Recently, it was also reported that the structure of another nucleosome construct forms around the TSS, known as the overlapping trinucleosome (OLTN), which is composed of octasome–hexasome–hexasome (21). However, an array different from the observed OLTN, such as octasome–tetrasome–hexasome or octasome–hexasome–tetrasome, has not yet been reported. It is assumed that the function of the SWI/SNF remodeler may be inequivalent between the octasome and hexasome because the OLDN and OLTN are formed by the function of the remodelers on the nucleosome array (6). The assumption was examined from the perspective of the accessibility of SWI/SNF remodelers to the subnucleosome moieties of the fluctuating OLDN as follows. First, BAF or PBAF, major members of SWI/SNF remodelers, were placed on the OLDN structures referring to cryoEM models of the remodeler-nucleosome core particle (NCP) complexes (PDB: 6LTJ, 7VDV) (22, 23). Because of the symmetry of the NCP structure, there are two ways to place the octasome of the OLDN at the NCP binding site of the remodelers. One way is to place the octasome so that the hexasome is above it (see Fig. 5A and C, denoted as side A). The other way is to arrange for the hexasome to be below the octasome (see Fig. 5A and C, denoted as side B). If the hexasome can also form a complex with the remodelers using the same NCP binding site, there can be two ways to place the hexasome. Therefore, four ways to place a moiety of the OLDN on the remodelers can be considered (Fig. S9). For every OLDN structure in the conformation ensemble, we constructed the four virtual BAF–OLDN complexes; the four virtual PBAF–OLDN complexes were constructed in a similar manner.

Next, the steric hindrance of the complex was evaluated using N_c, which is the number of contacting atom pairs between the remodeler and the OLDN. An excessively large N_c indicates a steric crash in the modeled complex, meaning that the complex cannot physically exist due to steric hindrance. In other words, the OLDN moiety cannot access the remodeler with its current orientation. Figure 5B and D shows the distribution of the averaged N_c values for the conformation ensemble of the OLDN. Asymmetric distributions were clearly observed depending on the remodeler–OLDN and their orientations. When BAF was placed in the octasome with the orientation of side A, the N_c value was almost zero in the region of the OLDN conformations with $R > 75$ Å (Fig. 5B, left). In the case where BAF was placed in the octasome with the side B orientation, the regions with small N_c values were localized to a narrow region where both θ and R were large. A high N_c value, exceeding 50, was observed uniformly across almost all regions of OLDN conformations when BAF was placed on either side of the hexasome (Fig. 5B). This implies that BAF can form a complex with the octasome of OLDN with a side A orientation, but it faces hindrance in accessing the hexasome of the OLDN. Similarly, the trend persisted in PBAF–OLDN complexes, where the N_c value for PBAF was close to zero in the region of OLDN conformations with $R > 80$ Å and $\theta > 10^{\circ}$, indicating an ability to access the octasome with a side A orientation (Fig. 5D, left). Moreover, when PBAF interacted with the octasome with a side B orientation or the hexasome, the N_c value was considerably large (Fig. 5D). We note that a region with small N_c also appeared around $R > 80$ Å in the case where PBAF was placed with the hexasome with side A orientation. For further validation of this trend, the N_c values were also calculated for the 12 cryoEM models. A similar tendency to the SAXS-based fluctuation was observed, where only four cases resulted in small N_c values. Specifically, when the octasomes of classes 07, 08, 09, and 11 were placed on the BAF with side A orientation, the N_c values were 37, 0, 0, and 20, respectively (Fig. 5A). Therefore, from an accessibility perspective, SWI/SNF remodelers are more likely to act on the octasome with a certain orientation than on the hexasome.

Discussion

In this study, we introduced an integrated approach combining cryoEM, SAXS, and CG-MD to investigate the fluctuations of biomolecules, subsequently applying this method to analyze the dynamics of OLDN. The acquisition of 12 sets of structural data by cryoEM allowed for the identification and characterization of structural fluctuations by comparing the distinct features present in each structure. However, techniques to visualize highly fluctuating molecules with cryoEM, such as chemical cross-linking, may introduce bias in the observed structures. In this regard, SAXS can provide complementary information, including bias-free structural information, on unstable and transient structures. Here, the MD simulation allowed for the extraction of individual structures and their distribution in the conformation ensemble from the SAXS data. In this study, the results of SAXS-based ensemble modeling with CG-MD simulations suggest that the fluctuation of the OLDN in solution is larger than the structural variability among the 12 cryoEM models. We note that the constraint of "The fluctuation includes the 12 cryoEM models" enabled us to visualize a reasonable ensemble model.

Frequently appearing structures are more likely to be detected in cryoEM imaging, and glutaraldehyde may cross-link two nucleosomal moieties that are sufficiently close to each other. Therefore, structures with less fluctuation—those with low potential energy—will tend to be obtained by cryoEM imaging. However, cryoEM analysis itself cannot address this presumption. In this study, our SAXS-based ensemble modeling with CG-MD simulations showed that the 12 cryoEM models of the OLDN are energetically stable among all possible fluctuation structures. This result supports the utility of the integrative approach of cryoEM, SAXS, and MD simulations as an effective tool for a comprehensive understanding of structural dynamics, including transient or rare structures. From the same perspective, structural analysis of complexed biomolecules combining cryoEM with other techniques, such as NMR or FRET, will also be effective.

In the current analysis, we revealed the asymmetric nature of structural fluctuations between octasomes and hexasomes. This observation suggests that factors beyond hexasome- or octasome-specific molecular surfaces could influence the binding to other proteins. Correspondingly, our analysis suggests a clear difference in accessibility to SWI/SNF remodelers between octasomes and hexasomes; the SWI/SNF remodelers can easily access octasomes while facing difficulties in accessing hexasomes. This asymmetry not only has implications for the formation process of OLDNs and OLTNs but may also provide insights into understanding the mechanism for overcoming transcriptional barriers. At present, no other proteins that bind to the OLDN have been identified. If such proteins are found in the future, their accessibility to the OLDN could be evaluated using the fluctuation model of the OLDN presented in this study.

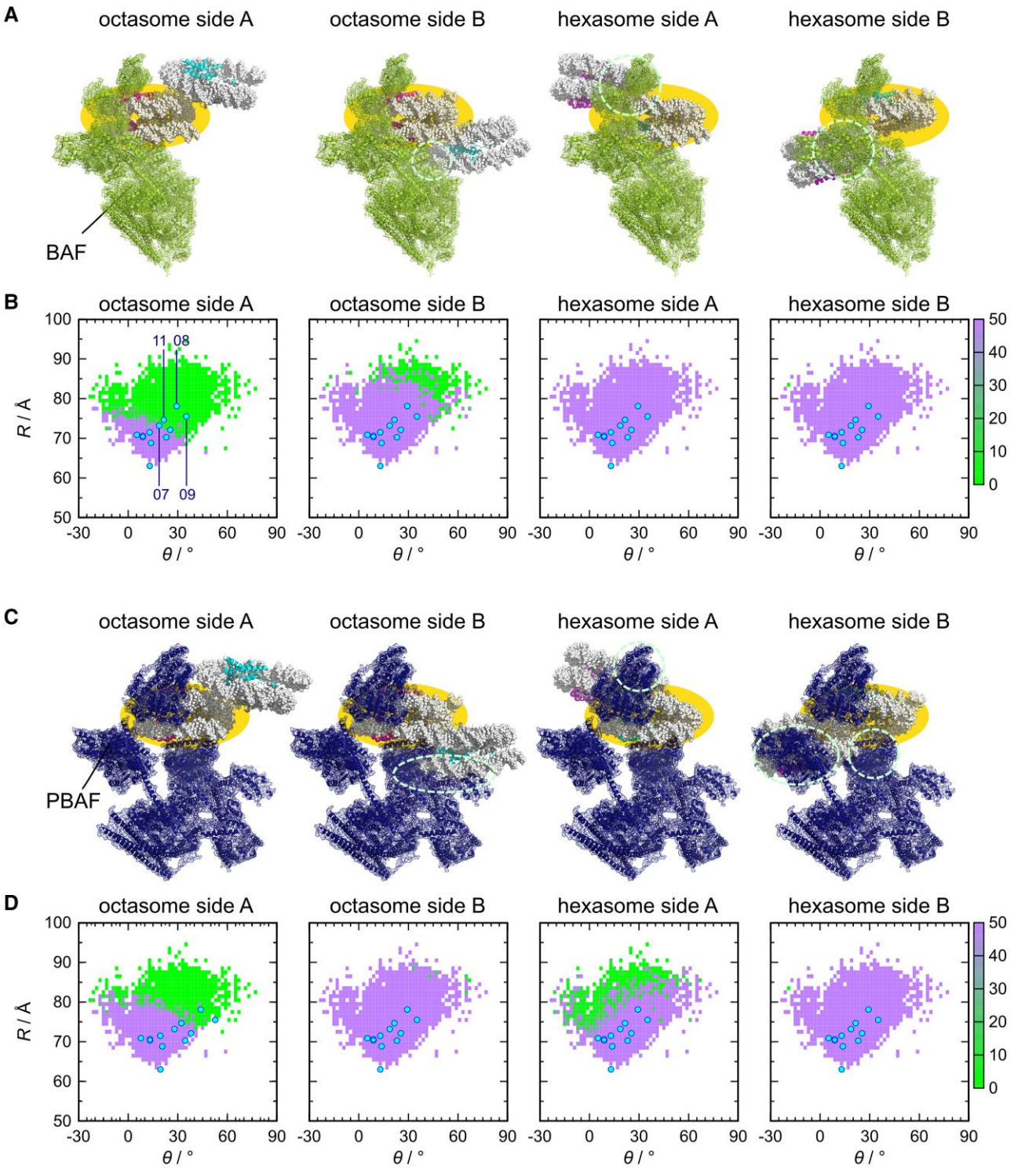

Fig. 5. Steric hindrance in virtual remodeler–OLDN complexes. A) Examples of BAF–OLDN complexes. There are four possible binding sites: octasome sides A and B and hexasome sides A and B. The orientation of BAF is the same throughout the four panels as the orientation of the OLDN changes. B) Averaged N_c value at each pixel. The colors indicate the values: green indicates low steric hindrance values, and purple indicates the opposite. C) Examples of PBAF–OLDN complexes. There are four possible binding sites: octasome sides A and B and hexasome sides A and B. The orientation of PBAF is the same throughout the four panels as the orientation of the OLDN changes. D) Averaged N_c values. In (A) and (C), OLDNs are drawn using the same color scheme as in Fig. 3D. BAF and PBAF are shown by yellowish green or dark blue ribbons and meshes, respectively. NCP binding sites in the remodelers are shown by yellow ellipses. The locations where the octasome or hexasome is in collision with the remodeler are indicated by the pale green dotted lines. In (B) and (D), the regions with $N_c > 50$ are drawn in the same color (purple). Here, the N_c was shown for pixels with an appearance probability >0.0001 in Fig. 3C. The locations of the 12 cryoEM models are shown by cyan circles.

In summary, characterizing fluctuations in a biomolecular complex enabled the discussion of its accessibility to other factors. As accessibility is an aspect of k_{on} or kinetics, the combination of cryoEM, SAXS, and MD simulations is expected to be a generic approach to bridge the gap between dynamics and kinetics. In addition, there are many experimental techniques that

complement the information obtained from cryoEM and SAXS. If more experimental data could be integrated, the accuracy of the structural fluctuation model could be improved.

Materials and methods

Preparation of the OLDN

The OLDN was prepared using 250-base pair DNA fragments derived from the Widom-601 sequence and a purified histone octamer, as previously described (8). Briefly, the histone octamer was mixed with a 2.8-fold molar ratio of the 250 base pair DNA fragments in a reconstitution buffer containing 10 mM Tris–HCl (pH 7.5), 2 M NaCl, 1 mM EDTA (pH 8.0), and 1 mM DTT. The NaCl concentration was then linearly reduced to 0.25 mM by continuous buffer exchange during dialysis for 33 h. The reconstituted OLDN was purified by nondenaturing gel electrophoresis using a PrepCell apparatus (Bio-Rad) in an elution buffer containing 20 mM Tris–HCl (pH 8.0) and 1 mM DTT. The eluted fractions were analyzed by nondenaturing PAGE, and the peak fractions were concentrated using an Amicon Ultra centrifugal filter unit (MWCO 30,000; Millipore). The resulting OLDN samples were stored on ice until further use.

Fixation of the OLDN for cryoEM analysis

Before blotting, the OLDN samples were fixed using the gradient fixation method (GraFix) (16). The gradient solutions (13.2 mL) containing 20 mM HEPES-KOH (pH 7.5), 50 mM KOAc, 0.2 μM $Zn(OAc)_2$, 0.1 mM TCEP (pH 8.0), 10–25% sucrose, and 0–0.1% glutaraldehyde (Electron Microscopy Sciences) in Ultra-Clear centrifuge tubes (Beckmann) were prepared using GRADIENT MASTER (BioComp). The purified OLDN was loaded on top of the gradient solution and was then centrifuged at 27,000 rpm for 16 h at 4 °C. After centrifugation, the sample aliquots were gently collected from the top of the gradient solution into 1.5-mL tubes, and the peak fractions were analyzed by nondenaturing gel electrophoresis with EtBr staining. The peak fractions were applied in a PD-10 column (Cytiva) and eluted with the final buffer containing 20 mM HEPES-KOH (pH 7.5), 50 mM KOAc, 0.2 μM $Zn(OAc)_2$, and 0.1 mM TCEP (pH 8.0). Finally, the eluted sample was concentrated with an Amicon Ultra centrifugal filter unit (MWCO 30,000; Millipore) and immediately used for blotting.

CryoEM data collection

For the preparation of cryoEM specimens, Quantifoil grids (R1.2/1.3, 200-mesh, copper, Quantifoil Micro Tools GmbH) were pretreated with ethyl acetate and glow-discharged in a soft plasma ion bombardment PIB-10 (Vacuum Device Inc.). Then, 2 μL aliquots (0.4 mg/mL of OLDN) were applied to the grids and blotted for 3 s (blot force, 5) under 100% humidity at 16 °C in Vitrobot Mark IV (Thermo Fisher Scientific). The grids were immediately immersed in liquid ethane and stored in grid boxes. CryoEM images were collected using a Tecnai Arctica transmission electron microscope (Thermo Fisher Scientific) equipped with a K2 summit direct electron detector (Gatan). Automated data collection was performed using SerialEM software (24).

Image processing

Single-particle analysis of the OLDN was performed with RELION3 software (Tables S1 and S2). First, motion correction and contrast transfer function estimation were performed with RELION3 (25) and Gctf (26), respectively. The particle images were automatically picked using the Laplacian-of-Gaussian filter. Contaminated junk particles were then removed throughout rounds of 2D and 3D classifications. De novo 3D model generation was used as a reference model for the initial 3D classification. After the final round of 3D classification, the four selected OLDN structures underwent a series of steps, including 3D auto-refine, Bayesian polishing, and another round of 3D auto-refine. Subsequently, multibody refinement (27) was performed using masks specific to the octasome and hexasome units. Composite maps were calculated for each class using phenix.combine_focused_maps (28).

Model building and refinement

Atomic models were built based on the crystal structure of the OLDN (PDB: 5GSE). First, the octasome and hexasome units were extracted from the previous crystal structure, and each unit was treated as a rigid block and fitted to the cryoEM maps using UCSF Chimera (29) for alignment. The linker DNA between the octasome and hexasome units was modeled manually using Coot (30). The models were automatically refined using phenix.real_space_refine (31) and manually edited using Coot. The models were validated by MolProbity (32).

Small-angle X-ray scattering

An OLDN solution was utilized at a concentration of 4.7 mg/mL in a buffer containing 20 mM Tris–HCl (pH 8.0), 50 mM NaCl, and 1 mM dithiothreitol. SAXS measurement was performed using NANOPIX (Rigaku, Japan) equipped with a point-focused Cu-Kα source generator (MicroMAX-007 HFMR, Rigaku, Japan) with a wavelength of 1.54 Å. The scattered X-rays were counted using a HyPix-6000 detector (Rigaku, Japan). The sample-to-detector distances were set at 1330 and 300 mm, covering a q-range of 0.008 $Å^{-1}$–0.70 $Å^{-1}$, where q is the magnitude of the scattering vector defined as $q = \left(4\pi \sin\frac{\phi}{2}\right)/\lambda$ with the scattering angle ϕ and the X-ray wavelength λ. The total exposure time was 500 min (50 accumulations of 10 min each). The circular average of the 2D scattering images to 1D profile was calculated using SAngler software (33) after data correction with background noise, transmitted X-ray intensity, and buffer scattering. The absolute scattering intensity calibration was made using the scattering intensity of water (1.632×10^{-2} cm^{-1}) as a standard.

Analytical ultracentrifugation

To estimate the amount of undesirable aggregated molecules, AUC was performed using the same solution that was used for the SAXS measurements. The sample solution was rotated at a speed of 40,000 rpm and a temperature of 25 °C using a sedimentation velocity method in both the interference and absorption modes. The acquired data were analyzed with the Lamm formula using SEDFIT software (https://sedfitsedphat.github.io/) (34). The sedimentation coefficient was converted to that at 20 °C in pure water ($s_{20,w}$), and the molecular weight was computed from $s_{20,w}$ and the friction ratio $f/f0$. We applied AUC-SAXS treatment to eliminate the influence of aggregated molecules from the experimental SAXS profile (Fig. S3). Details of the AUC-SAXS treatment have been described elsewhere (16, 17).

Dynamic light scattering

DLS measurement was performed using a system equipped with a 22-mW He–Ne laser, an avalanche photodiode (APD, ALV, Germany) mounted on a static/dynamic compact goniometer, ALV/LSE-5003 electronics, and an ALV-5000 correlator

(ALV-Laser Vertriebsgesellschaft GmbH, Langen, Germany). Measurement was performed at a temperature of 293 K, and CONTIN analyses were conducted to obtain the distribution of relaxation rates at eight different q values.

NMA optimization

NMA optimization was performed using Pepsi-SAXS software (version 3.0, Linux) (18, 19). The details are described in the SI Appendix.

Modeling the OLDN with full-length histone proteins

The atomistic model of the OLDN with full-length histone proteins was created by connecting the N- and C-terminal flexible regions (histone tails). First, full-length histone proteins were prepared using homology modeling. The one-to-one threading mode of the Phyre2 modeling server (35) was employed, referring to the crystal structure of PDB: 1KX5 (36). Second, the coordinates of the missing N- and C-terminal regions were compensated for using homology models. Different methods were employed for the cryoEM models and for the models after NMA optimization. For the cryoEM models, the homology-modeled histone octamer or hexamer was superimposed onto the cryoEM models, and then the proteins in the cryoEM models were replaced with the homology model. For models after NMA optimization, each missing N- or C-terminus was compensated for (one by one) using N- or C-terminal fragments from the homology models. Each fragment included an overlap of 10 amino acids with the NMA-optimized model. Each fragment was superposed onto the corresponding NMA-optimized model, and full-length histone proteins were modeled.

CG-MD simulation

The CG-MD simulations were performed using CafeMol 3.2.1 (37). The AICG2+ protein model and 3SPN.2 DNA model were employed, where each amino acid and each of the sugar, base, and phosphate groups of DNA were represented by a single bead (38, 39). In addition, the Debye–Hückel type electrostatic interaction, excluded volume effect, and inter DNA-protein Go potential were included. The default parameters of CafeMol 3.2.1 were used unless otherwise stated. The AICG2+ and Go potentials were employed to reproduce the tertiary structures of the hexasome and octasome, where the cryoEM structure class 09 was used as a reference. Native contact potentials were defined only for the amino acid beads within the folded region, as well as for sugar and base beads. Here, the folded region denotes the region where the atomic coordinates were identified in all 12 cryoEM models. The flexible dynamics of the other regions were expressed using a flexible local potential (40). Charges were defined in different ways depending on the region. For the folded region, the charge of each bead was defined using RESPAC (41). For the other regions, each lysine, arginine, glutamic acid, aspartic acid, and phosphate was treated as +1.0, +1.0, −1.0, −1.0, and −0.6 charged bead, respectively. The ionic strength was set to 0.15. Meanwhile, CGMD simulations at various ionic strengths were also performed to investigate the ionic strength dependence of the ensemble model (shown in Fig. S8).

Langevin dynamic simulations were performed for 50,000,000 steps at 300 K, with a time step of 0.2 CafeMol time units. Ten simulations were performed by changing the random seeds. The initial structure was prepared by performing steepest descent energy minimization for cryoEM model class 09 with its histone tails compensated for. The procedure of the compensation is described in the SI Appendix. Simulation snapshots were recorded every 10,000 steps. To conduct structural analysis using atomic coordinates, each CG-MD snapshot was converted into an atomistic model using BBQ (42), Scwrl4 (43), and DNA backmap (44). The SAXS profiles of the CG-MD snapshots were calculated using Pepsi-SAXS (18, 19).

Ensemble modeling

The initial ensemble contained all the CG-MD snapshots with the same weight. The structural ensemble that reproduced the experimental SAXS profile was constructed by repeatedly changing the weights of the snapshots in the initial ensemble as follows:

Step 1: Select a snapshot to change the weight. The snapshot was chosen based on $\frac{\Delta\chi^2}{\Delta KL}$ after slightly decreasing its weight (1% of the initial weight). Here, $\chi^2 = \frac{1}{n-1}\sum_{i=1}^{n}\left(\frac{I_{exp}(q_i) - cI_{ens}(q_i)+a}{\sigma(q_i)}\right)^2$, where c and a are parameters that minimize χ^2. In addition, $KL = \sum_{j=1}^{m} p_{cur}(j)\ln\frac{p_{cur}(j)}{p_{ini}(j)} = \sum_{j=1}^{m}\frac{w_{cur}(j)}{W_{cur,sum}}\ln\frac{\frac{w_{cur}(j)}{W_{cur,sum}}}{\frac{w_{ini}(j)}{W_{ini,sum}}}$, where m, $p_{cur}(j)$, $p_{ini}(j)$, $w_{cur}(j)$, and $w_{ini}(j)$ are the number of snapshots, fraction of the jth snapshot in the current structural ensemble, fraction of the snapshot in the initial structural ensemble, weight of the jth snapshot in the current structural ensemble, and weight in the initial structural ensemble (in this study, $w_{ini}(j) = 1.0$), respectively. In addition, the $W_{cur,sum}$ and $W_{ini,sum} = \sum_{j=1}^{m} w_{ini}(j)$ are defined by $W_{cur,sum} = \sum_{j=1}^{m} w_{cur}(j)$ and $W_{ini,sum} = \sum_{j=1}^{m} w_{ini}(j)$, respectively. For the hth snapshot, $\Delta\chi^2$ and ΔKL represent the difference in χ^2 and KL before and after decreasing the weight of the hth snapshot, respectively. The $\frac{\Delta\chi^2}{\Delta KL}$ was calculated for all snapshots, and the snapshots were ranked for selection according to the following criteria: (i), a snapshot with negative values of $\Delta\chi^2$ (χ^2 decreases after reweighting) was chosen; (ii), snapshots with positive ΔKL values (KL increases after reweighting) were prioritized over those with negative ΔKL values; and (iii), higher priority was assigned to a snapshot with a larger value of $\frac{\Delta\chi^2}{\Delta KL}$.

Step 2: The weight of the selected snapshot was decreased by 1% of its initial weight. The reweighting was repeated until the $\Delta\chi^2$ fell below 3.0.

Calculation of N_c

The octasome or hexasome of the OLDN was superimposed onto the NCP in the BAF–NCP or PBAF–NCP complex (PDB: 6LTJ, 7VDV). The regions used for superposition were Cα atoms in Leu60-Gly132 of histone H3, Asn25-Gln93 of histone H4, Thr16-Pro109 of histone H2A, and Ser36-Thr122 of histone H2B. When the octasome was superimposed onto the BAF–NCP or PBAF–NCP complex, the N_c was defined as the number of contacting atom pairs between the hexasome and the remodeler. When the hexasome was superimposed onto the BAF–NCP or PBAF–NCP complex, the N_c was defined as the number of contacting atom pairs between the octasome and the remodeler. Since histone tails are flexible, they were ignored in the calculation of the contacting pairs. The regions analyzed for calculating N_c are shown in Table S3.

Acknowledgments

The cryoEM experiments were performed with the Tecnai Arctica microscope at the RIKEN Yokohama cryoEM facility.

We thank Dr. S. Grudinin for the helpful advice on the use of Pepsi-SAXS (NMA optimization software). We also thank the staff of the Radiation Material Science Laboratory of the Institute for Integrated Radiation and Nuclear Science, Kyoto University (KURNS), for their assistance with the SAXS and AUC experiments.

Supplementary Material

Supplementary material is available at *PNAS Nexus* online.

Funding

This work was supported by MEXT/JSPS KAKENHI under Grant Nos. JP18H05229, JP18H03681 and JP18H05534 (M.Su.); JP23H05475 and JP24H02328 (H.K.); JP24K18081 (M.Sh.); JP22K06098 (Y.T.); 23H02519 (K.N); JP19K16088 and JP21K15051 (K.M.); JP19KK0071 and JP20K06579 (R.I.); by the Research Support Project for Life Science and Drug Discovery (Basis for Supporting Innovative Drug Discovery and Life Science Research) from AMED under Grant Nos. 24ama121001j0003 (M.Su.) and JP24ama121009 (H.K.); by JST ERATO under Grant No. JPMJER1901 (H.K.); by JST CREST Grant No. JPMJCR24T3 (H.K.); by JST FOREST under Grant No. JPMJFR224Z (K.N.); by the Research Fund for Young Scientists in Kyoto University (K.M.); by the Fund for Project Research in Institute for Integrated Radiation and Nuclear Science, Kyoto University (K.M.); and by The Joint Usage/Research of the Institute for Integrated Radiation and Nuclear Science, Kyoto University (KURNS) under Grant Nos. R3069 and R4010 (K.M.). The project for construction of the basis for advanced materials science and analytical studies by innovative use of quantum beams and nuclear sciences in KURNS.

Author Contributions

Conceptualization: M.Su., H.K.; Methodology: M.Su., H.K., M.Sh., H.T., M.N., and N.S.; Investigation: M.Sh., H.T., M.N., N.S., K.N., H.E., S.S., K.M., R.I., and Y.T.; Project administration: K.M., N.S., and H.K.; Supervision: M.Su. and H.K.; Writing—original draft: M.Su., H.K., M.Sh., H.T., and N.S.; Writing—review & editing: K.N., H.E., S.S., K.M., R.I., Y.T., H.K., and M.Su.

Data Availability

The authors confirm that the data supporting the findings of this study are available within the article and/or its supplementary materials. All simulation trajectories are available at the Zenodo repository (https://doi.org/10.5281/zenodo.13955263).

References

1 Oudelaar AM, Higgs DR. 2021. The relationship between genome structure and function. *Nat Rev Genet*. 22:154–168.
2 Wolffe A. 1999. *Chromatin: structure and function*. 3rd ed. San Diego: Academic.
3 Kornberg RD, Thomas JO. 1974. Chromatin structure; oligomers of the histones. *Science* 184:865–868.
4 Luger K, Mäder AW, Richmond RK, Sargent DF, Richmond TJ. 1997. Crystal structure of the nucleosome core particle at 2.8 Å resolution. *Nature* 389:251–260.
5 Teves SS, Weber CM, Henikoff S. 2014. Transcribing through the nucleosome. *Trends Biochem Sci*. 39:577–586. 10.1016/j.tibs.2014.10.004
6 Lorch Y, LaPointe JW, Kornberg RD. 1987. Nucleosomes inhibit the initiation of transcription but allow chain elongation with the displacement of histones. *Cell* 49:203–210.
7 Ulyanova NP, Schnitzler GR. 2005. Human SWI/SNF generates abundant, structurally altered dinucleosomes on polynucleosomal templates. *Mol Cell Biol*. 25:11156–11170.
8 Kato D, *et al.* 2017. Crystal structure of the overlapping dinucleosome composed of hexasome and octasome. *Science* 356:205–208.
9 Matsumoto A, *et al.* 2020. Structural studies of overlapping dinucleosomes in solution. *Biophys J*. 118:2209–2219.
10 Ehara H, Kujirai T, Shirouzu M, Kurumizaka H, Sekine SI. 2022. Structural basis of nucleosome disassembly and reassembly by RNAPII elongation complex with FACT. *Science* 377:eabp9466.
11 Yunoki Y, *et al.* 2022. Overall structure of fully assembled cyanobacterial KaiABC circadian clock complex by an integrated experimental-computational approach. *Commun Biol*. 5:184.
12 Kassem N, *et al.* 2021. Order and disorder-an integrative structure of the full-length human growth hormone receptor. *Sci Adv*. 7:eabh3805.
13 Jussupow A, *et al.* 2020. The dynamics of linear polyubiquitin. *Sci Adv*. 6:eabc3786.
14 Chen Y, *et al.* 2017. Asymmetric unwrapping of nucleosomal DNA propagates asymmetric opening and dissociation of the histone core. *Proc Natl Acad Sci U S A*. 114:334–339.
15 Shimizu M, *et al.* 2022. Extracting time series matching a small–angle X-ray scattering profile from trajectories of molecular dynamics simulations. *Sci Rep*. 12:9970.
16 Kastner B, *et al.* 2008. GraFix: sample preparation for single-particle electron cryomicroscopy. *Nat Methods*. 5:53–55.
17 Morishima K, *et al.* 2020. Integral approach to biomacromolecular structure by analytical-ultracentrifugation and small-angle scattering. *Commun Biol*. 3:294.
18 Morishima K, Inoue R, Sugiyama M. 2023. Derivation of the small-angle scattering profile of a target biomacromolecule from a profile deteriorated by aggregates. AUC-SAS. *J Appl Crystallogr*. 56:624–632.
19 Grudinin S, Garkavenko M, Kazennov A. 2017. Pepsi-SAXS: an adaptive method for rapid and accurate computation of small-angle X-ray scattering profiles. *Acta Crystallogr D Struct Biol*. 73:449–464.
20 Larsen AH, *et al.* 2020. Combining molecular dynamics simulations with small-angle X-ray and neutron scattering data to study multi-domain proteins in solution. *PLoS Comput Biol*. 16:e1007870.
21 Nishimura M, *et al.* 2024. Genome-wide mapping and cryo-EM structural analyses of the overlapping tri-nucleosome composed of hexasome-hexasome-octasome moieties. *Commun Biol*. 7:61.
22 He S, *et al.* 2020. Structure of nucleosome-bound human BAF complex. *Science* 367:875–881.
23 Yuan J, Chen K, Zhang W, Chen Z. 2022. Structure of human chromatin-remodelling PBAF complex bound to a nucleosome. *Nature* 605:166–171.
24 Mastronarde DN. 2005. Automated electron microscope tomography using robust prediction of specimen movements. *J Struct Biol*. 152:36–51.
25 Zivanov J, *et al.* 2018. New tools for automated high-resolution cryo-EM structure determination in RELION-3. *eLife* 7:e42166.
26 Zhang K. 2016. Gctf: real-time CTF determination and correction. *J Struct Biol*. 193:1–12.
27 Nakane T, Kimanius D, Lindahl E, Scheres SH. 2018. Characterisation of molecular motions in cryo-EM single-particle data by multi-body refinement in RELION. *eLife* 7:e36861.

28 Liebschner D, *et al*. 2019. Macromolecular structure determination using X-rays, neutrons and electrons: recent developments in Phenix. *Acta Crystallogr D Struct Biol*. 75:861–877.
29 Pettersen EF, *et al*. 2004. UCSF Chimera—a visualization system for exploratory research and analysis. *J Comput Chem*. 25: 1605–1612.
30 Emsley P, Lohkamp B, Scott WG, Cowtan K. 2010. Features and development of coot. *Acta Crystallogr D Biol Crystallogr*. 66:486–501.
31 Afonine PV, *et al*. 2018. Real-space refinement in PHENIX for cryo-EM and crystallography. *Acta Crystallogr D Struct Biol*. 74: 531–544.
32 Williams CJ, *et al*. 2018. MolProbity: more and better reference data for improved all-atom structure validation. *Protein Sci*. 27: 293–315.
33 Shimizu N, *et al*. 2016. Software development for analysis of small-angle X-ray scattering data. *AIP Conf Proc*. 1741:050017.
34 Schuck P. 2000. Size-distribution analysis of macromolecules by sedimentation velocity ultracentrifugation and Lamm equation modeling. *Biophys J*. 78:1606–1619.
35 Kelley LA, Mezulis S, Yates CM, Wass MN, Sternberg MJ. 2015. The Phyre2 web portal for protein modeling, prediction and analysis. *Nat Protoc*. 10:845–858.
36 Davey CA, Sargent DF, Luger K, Maeder AW, Richmond TJ. 2002. Solvent mediated interactions in the structure of the nucleosome core particle at 1.9Å resolution. *J Mol Biol*. 319: 1097–1113.
37 Kenzaki H, *et al*. 2011. CafeMol: a coarse-grained biomolecular simulator for simulating proteins at work. *J Chem Theory Comput*. 7:1979–1989.
38 Li W, Wang W, Takada S. 2014. Energy landscape views for interplays among folding, binding, and allostery of calmodulin domains. *Proc Natl Acad Sci U S A*. 111:10550–10555.
39 Hinckley DM, Freeman GS, Whitmer JK, de Pablo JJ. 2013. An experimentally-informed coarse-grained 3-site-per-nucleotide model of DNA: structure, thermodynamics, and dynamics of hybridization. *J Chem Phys*. 139:144903.
40 Terakawa T, Takada S. 2011. Multiscale ensemble modeling of intrinsically disordered proteins: p53 N-terminal domain. *Biophys J*. 101:1450–1458.
41 Terakawa T, Takada S. 2014. RESPAC: method to determine partial charges in coarse-grained protein model and its application to DNA-binding proteins. *J Chem Theory Comput*. 10:711–721.
42 Gront D, Kmiecik S, Koliński A. 2007. Backbone building from quadrilaterals: a fast and accurate algorithm for protein backbone reconstruction from alpha carbon coordinates. *J Comput Chem*. 28:1593–1597.
43 Krivov GG, Shapovalov MV, Dunbrack RL, Jr. 2009. Improved prediction of protein side-chain conformations with SCWRL4. *Proteins* 77:778–795.
44 Shimizu M, Takada S. 2018. Reconstruction of atomistic structures from coarse-grained models for protein–DNA complexes. *J Chem Theory Comput*. 14:1682–1694.